Manuscript pages : 18;
Submitted to ApJ on November 16, 2015

Reflected Light Curves, Spherical and Bond Albedos of Jupiter- and Saturn-like Exoplanets

Ulyana Dyudina[1], Xi Zhang[2], Liming Li[3], Pushkar Kopparla[1], Yuk L. Yung[1], Andrew P. Ingersoll[1], Luke Dones[4]

(1)Division of Geological and Planetary Sciences, 150-21 California Institute of Technology, Pasadena, CA 91125 (U.S.A.) (2) University of California Santa Cruz 1156 High St, Santa Cruz, CA 95064, (U.S.A.) (3) Department of Physics, University of Houston, Houston, TX 77204, (U.S.A) (4) Southwest Research Institute, 1050 Walnut St., Suite 400, Boulder CO 80302 (U.S.A.)

ABSTRACT

We estimate how the light curve and total stellar heating of a planet depend on forward and backward scattering clouds. To do that, we construct light curves for Jupiter- and Saturn-like planet based on observations. We fit analytical functions to the reflected brightness of Jupiter's and Saturn's surface versus planet's phase. We use Pioneer and Cassini spacecraft images to estimate these functions. These observations cover broad bands at 0.59-0.72 μm and 0.39-0.5 μm, and narrow bands at 0.938 μm (atmospheric window), 0.889 μm (CH_4 absorption band), and 0.24-0.28 μm. We simulate the images of the planets at different phases with ray-tracing model of a planet by Dyudina et al. (2005). The full-disk luminosity of these simulated images changes with planet's phase producing the full-orbit light curves. We also derive total planet's reflection integrated in all directions (spherical albedos) for Jupiter, Saturn, and for planets with Lambertian and Rayleigh-scattering atmosphere. For Jupiter, we tune the model to fit the observed full-disk brightness at several phase angles. Jupiter-like atmosphere can produce light curves that are a factor of two fainter at half-phase than the Lambertian planet, given the same geometric albedo at transit. The spherical albedo (and likely the wavelengh-integrated Bond albedo) is lower than for a Lambertian planet. Corresponding absorption of the stellar light and the planet's heating rate

[1]Division of Geological and Planetary Sciences, 150-21 California Institute of Technology, Pasadena, CA 91125 (U.S.A.), ulyana@gps.caltech.edu

would be higher than for a grey Lambertian planet. Lambertian assumption can overestimate spherical albedo by up to a factor of ∼1.5.

Subject headings: methods: data analysis; planets and satellites: surfaces; planets and satellites: Jupiter; planets and satellites: Saturn; planets and satellites: detection; scattering

1. Introduction

In the last decade thermal light curves and secondary eclipses were observed for more than 50 transiting exoplanets, and 5 were directly imaged (Madhusudhan et al. 2014). Most of these observations are either time-varying signals (transits, secondary eclipses, and phase curves), or spatially resolved imaging and spectroscopy. These techniques allow one to study the relative abundances of common elements such as C, H, O, and N, corresponding atmospheric chemistries, vertical pressure-temperature profiles, global circulation patterns, and clouds, which block the emission from the planets and screen the planet from the star's heating.

The first phase curves of exoplanets showed thermal emission. Starting with non-transiting planets υ Andromedae b at 24μm (Harrington et al. 2006) and HD 179949 at 8μm (Cowan et al. 2007), and transiting hot Jupiter HD 189733b at 8μm (Knutson et al. 2007), phase curves have been detected for about a dozen planets, two of them on eccentric orbits. Visible-wavelength light curves were detected for three planets. At these visible wavelengths the phase curve is the sum of the thermal and reflected light components, and infrared observations are required to distinguish between the two. Demory et al. (2013) identified the reflected nature of the phase curve of hot Jupiter Kepler-7b by comparing it to the 3.6 and 4.5μm *Spitzer* observation, showing that the planet is highly reflective. Its geometric albedo (the ratio of planet's reflected flux to that of a same-size flat Lambertian disk) is $A_g = 0.35 \pm 0.02$. Another detection of blue-colored reflective ($A_g = 0.4 \pm 0.12$) hot Jupiter HD 189733b comes from the secondary eclipse (Evans et al. 2013). High reflectivity suggest clouds, which may originate from condensation of silicates or other "rocky" materials, or from photochemical processes. Most hot Jupiters have albedos less than 0.1, but a subset have much larger albedos around 0.3 (Heng and Demory 2013). This group includes both Kepler-7 and HD 189733b.

Unpolarized reflected light from Jupiter and Saturn analogs is too faint for detection in the near future (the relative planet to star flux ratio $F/F_* \sim 10^{-8} - 10^{-9}$, or 0.001-0.01 ppm). The reflected light from hot Jupiters is detected at the levels $F/F_* \sim 10^{-4} - 10^{-5}$.

The detections indicate albedos up to $A_g \sim 0.4$, which requires clouds. Though clouds on Jupiter and Saturn form at different temperatures, larger pressures, from different chemical elements, and are somewhat brighter ($A_g \sim 0.5 - 0.6$), they represent multiple scattering on relatively bright cloud particles, as on hot Jupiters. The spectrum of the clouds on Jupiter and Saturn, sampled in atmospheric windows, is surprisingly featureless. These clouds act as spectrally flat scatterers, whose brightness depends on the particle size, albedo, and density, but not on composition. Accordingly, clouds on extrasolar planets may have similar scattering properties in atmospheric windows, even though different gases above the clouds can result in different spectra. Models of cloud distribution on Jupiter and Saturn from observations give a wide range of possible cloud properties (reviewed by West et al. 2004, 2009). Application of cloud models to disk-integrated planet's luminosity, which is needed for orbital light curves, inherits the uncertainty.

This paper is the first to use the Cassini Jupiter flyby visible images to construct Jupiter's light curve. This data set has the best phase angle coverage among spacecraft observations. We also use published data from previous spacecraft that visited Jupiter and Saturn. The most complete published data on the reflectance of Jupiter's and Saturn's cloud top "surfaces" come from Pioneer 10 and 11 (Tomasko et al. 1978; Smith and Tomasko 1984; Tomasko and Doose 1984). The reflectances were measured for two wavelengths bands (red and blue). The phase angle dependence of the reflectances was used to reconstruct light curves of a planet similar to Jupiter and Saturn using a 3D model of a planet with or without rings (Dyudina et al. 2005). Jupiter's and Saturn's atmospheres show strong backward and forward scattering. As a result the light curve shapes were substantially different from the Lambertian case.

We also derive planet's spherical albedo at various wavelength bands - the reflective property closely related to Bond albedo, which characterizes total reflected flux from the planet. Bond albedo for extrasolar planets had been roughly estimated from their visible luminocities at secondary eclipse and from the flux radiated in infrared (Schwartz and Cowan 2015). The poorly restricted relation of Bond albedo to secondary eclipse luminosity is addressed in this paper using Jupiter and Saturn as examples.

We derive light curves from Cassini Jupiter flyby images. We also use surface reflectance phase functions derived by Dyudina et al. (2005) from Pioneer data (Tomasko et al. 1978; Smith and Tomasko 1984). The planet model and the planets' measured reflectances are described in Section 2. The light curves modeled for different wavelength bands are shown in Section 3. The planet-integrated reflected light (spherical albedos) for Jupiter and Saturn at different wavelength bands, and the range of possible stellar heating for extrasolar cloud-covered planets are discussed in Section 4. Possible implications of our results for the

extrasolar planets are discussed in Section 5.

2. Model

We simulate planet images by tracing plane-parallel light rays from the distant central star reflected by each position on the planet (Dyudina et al. 2005). This produces images (80 pixels across the planet's disk). In this work the planet is spherical. The wavelengths in our model are integrated across the transmissivity of the Pioneer and Cassini filters. Our notation matches that of most observational papers on Saturn and Jupiter; the notation details can be found in Dyudina et al. (2005). The variables we use in this paper are defined in Table 1.

Variable	Description	Units (if any)
A, B	Coefficients of the Backstorm law (Eq. 4)	
A_b	Bond albedo	
A_g	Geometric albedo	
A_{HG}	Coefficient of Henyey-Greenstein function	
A_S	Spherical albedo	
F	Intensity of a white Lambertian surface[a]	$Wm^{-2}sr^{-1}$
g_1, g_2, f	Parameters of double Henyey-Greenstein function	
I	Intensity (or brightness, or radiance) of the surface	$Wm^{-2}sr^{-1}$
L_P	Luminosity of the planet[b]	Wsr^{-1}
L_*	Luminosity of the star[b]	Wsr^{-1}
$p(\alpha)$	Full-disk albedo[b c] $L_P/(\pi R_P^2 F)$	
R_P	Radius of the planet	km
$r_{\rm pix}$	Pixel size	km
α	Phase angle	degrees
Θ	Orbital angle ($\pm 180°$: min phase, $0°$: max phase)	degrees
μ_0, μ	Cosines of the incidence and emission angle	

Table 1: Variables used in our modeling. The detailed definitions follow in the text.

[a] $F \cdot (\pi$ steradians) is the incident stellar flux at the planet's orbital distance (which is also sometimes called F, but has Wm^{-2} units unlike our intensity F measured per unit solid angle).

[b] The optical properties for particular filters are the convolution of the planet's spectrum with the wavelength-dependent filter transmissivity.

[c] The "full disk albedo" term is adopted from Karkoschka (1998). It is related to the variable Ψ used by Seager and Deming (2010): $\Psi = \pi \cdot p(\alpha)$

2.1. Reflecting properties of Jupiter, Saturn, Lambertian and Rayleigh-scattering planets.

We study the light curves and total solar absorbed light as it depends on scattering by the planet's cloudy surface. We do not distinguish altitudes at which clouds scatter the light, but use the observed planet's brightness representing light scattered by an entire atmospheric column. We test a set of analytical functions describing surface scattering of Jupiter and Saturn, fitted to spacecraft observations, and compare them to Lambertian scattering, and to modeled semi-infinite Rayleigh-scattering atmosphere with particle's single scattering albedo 0.999999 and 0.3 (Kopparla et al. 2015). When possible, we use published data on the planet's surface scattering, e.g., the already fitted analytical function for Saturn's surface by Dones et al. (1993). For Jupiter the surface scattering measurements were fitted to the cloud model by (Tomasko et al. 1978) in order to derive single scattering phase function of cloud particles. We do not attempt to fit cloud distribution to Pioneer observations. Instead we fit analytical functions to the reflectance data points published by Tomasko et al. (1978) and then use these functions to simulate full-disk images.

2.1.1. Jupiter

Each location on Jupiter's surface is assumed to reflect solar light in the same way, i.e., our analytical reflectance function is uniform over the planet. In general, the reflected light depends on three angles: incidence (via cosine of incidence angle μ_0), emission (via cosine of emission angle μ), and phase angle α. In our notation, the phase angle $\alpha = 0^\circ$ indicates backward scattering and $\alpha = 180^\circ$ indicates forward scattering. We ignore the dependence on μ and assume brightness proportional to μ_0 for Jupiter because, as we will show, this simplification can give a reasonably good fit to the data.

We fit an analytical function to image pixel brightness in the units of I/F.

$$I(\alpha, \mu_0, \mu)/F \approx \mu_0 \cdot P(A_{HG}, g_1, g_2, f, \alpha). \quad (1)$$

$I(\alpha, \mu, \mu_0)$ is the reflected intensity at given location the planet. μ_0 is the cosine of the incidence angle measured from the local vertical. $F \cdot \mu_0$ is the reflected brightness of a white Lambertian surface. $F \cdot (\pi$ steradians) is a solar flux at the planet's orbital distance. $P(A_{HG}, g_1, g_2, f, \alpha)$ is a two-term Henyey-Greenstein function.

$$P(A_{HG}, g_1, g_2, f, \alpha) = A_{HG} \cdot (f P_{HG}(g_1, \alpha) + (1 - f) P_{HG}(g_2, \alpha)) \quad (2)$$

The coefficient A_{HG} is fitted to match the amplitude of the observed phase function. The individual terms P_{HG} are Henyey-Greenstein functions representing forward and backward

scattering lobes, respectively.

$$P_{HG}(g,\alpha) \equiv \frac{(1-g^2)}{(1+g^2+2g\cdot\cos\alpha)^{3/2}} \quad , \tag{3}$$

where α is the phase angle, $f \in [0,1]$ is the fraction of the forward versus backward scattering, and g is one of g_1 or g_2; $g_1 \in [0,1]$ controls the sharpness of the forward scattering lobe while $g_2 \in [-1,0]$ controls the sharpness of the backscattering lobe.

A commonly-used for surface reflection Bidirectional Reflection Distribution Function (BRDF) can be expressed in variables of Eq. 1 as: BRDF $= I(\alpha,\mu_0,\mu)/(\pi F \mu_0)$. Accordingly, our double Henyey-Greenstein function approximation is a scaled BRDF: BRDF $\approx P(A_{HG},g_1,g_2,f,\alpha)/\pi$. Note that typically the Henyey-Greenstein function is used for single-particle scattering, and then the function is normalized over the emission solid angles to give a unit single scattering albedo. Here we use this function only as a convenient analytical expression to fit the measured multiple scattering of Jupiter's cloud surface, for which particles' single scattering albedo is not relevant. In our case, the value to normalize to is the spherical albedo (the ratio of reflected to incident light for the whole planet at appropriate wavelengths). It is imbedded in the Henyey-Greenstein function. We will calculate the spherical albedo later in this paper.

Figure 1 shows our fits of Henyey-Greenstein functions to the image pixel values divided by μ_0 taken from Pioneers 10 and 11 flybys (Tomasko et al. 1978; Smith and Tomasko 1984). The corresponding Henyey-Greenstein coefficients are given in Table 2. The solid line was used by Dyudina et al. (2005) to fit the black data points (red filter) in Fig. 1. In this paper we also show the dotted and dashed curves, which represent the range of functions that are visually consistent with the range of black data points in Fig. 1.

Pioneer images show that different surface locations on Jupiter have different scattering properties. In particular, Tomasko et al. (1978) and Smith and Tomasko (1984) indicate two types of locations: the belts, usually seen as dark bands on Jupiter, and zones, usually seen as bright bands on Jupiter. The relative calibration between Pioneer 10 and Pioneer 11 data is not as well constrained as the calibration within each data set. Our model curve better represents the observations in the red filter (black data points) than in the blue filter. The Pioneer 11 blue data points at moderate phase angles $\alpha \sim 30-80^\circ$ (P11 in Fig. 1) seem to be systematically offset up from the Pioneer 10 (P10) blue data points, which may be a result of relative calibration error, or temporal change in clouds. Because of that, we do not model the blue wavelengths. Red wavelengths may also have that problem, though it is not so obvious in Fig. 1 (black data points). Accordingly, the red phase function derived by Dyudina et al. (2005) (black solid curve in Fig. 1) is also uncertain. However, after disk averaging, this fitted function reproduces the full-disk brightness observed by HST

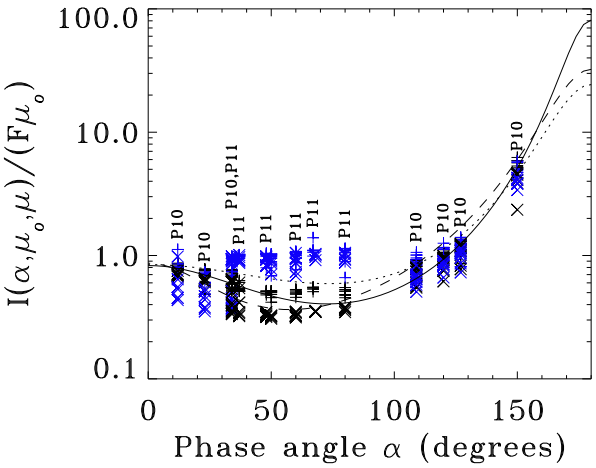

Fig. 1.— Fits of Henyey-Greenstein functions to the Pioneer 10 data, labeled P10 (Tomasko et al. 1978), and Pioneer 11 data, labeled P11 (Smith and Tomasko 1984). The data represent belts (× symbols) and zones (+ symbols) on Jupiter observed with the red (0.595–0.720 μm, black symbols) and blue (0.390–0.500 μm, blue symbols) filters. The solid, dashed and dotted lines demonstrate the range of possible fits to the red filter points (black symbols).

Spacecraft	Year	Filter	Wavelength	Linestyle	A_{HG}	g_1	g_2	f
Pioneers 10,11	1973,1974	red	0.595-0.72 μm	solid	2	0.80	-0.38	0.90
				dashed	1.80	0.70	-0.55	0.95
				dotted	1.60	0.70	-0.25	0.80
Cassini	2000-2001	CB3	0.938 μm	solid	0.95	0.55	-0.30	0.75
				dashed	1.20	0.70	-0.40	0.85
				dotted	0.95	0.35	-0.10	0.60
Cassini	2000-2001	MT3	0.889 μm	solid	0.09	0.40	-0.30	0.80
				dashed	0.11	0.30	-0.50	0.95
				dotted	0.10	0.35	-0.25	0.85
Cassini	2000-2001	UV1	0.258 μm	solid	0.40	0.40	-0.50	0.95
				dashed	0.60	0.60	-0.60	0.96
				dotted	0.50	0.40	-0.30	0.93

Table 2: Henyey-Greenstain coefficients fitted to Pioneer and Cassini Jupiter data.

(Karkoschka 1994, 1998) at the red passband of Pioneer filters. To explore the effects of the Pioneer 10/11 uncertainty in red wavelengths we fit two other curves (dotted and dashed) to the data.

Figure 2 shows our fits of the Henyey-Greenstain functions (panels a,c,e) to the data from the Cassini images of Jupiter. The functions are fitted in the atmospheric window (938 nm CB3 filter), strong CH_4 absorption band (889 nm MT3 filter), and in UV (258 nm UV1 filter). The filter details can be found in (Porco et al. 2004). The fitted Henyey-Greenstein parameters are listed in Table 2. The data points represent a variety of incidence and emission angles. The high-latitude data points (orange in Fig. 2) are illuminated and observed at very slanted angles during the equatorial Cassini flyby. These points are systematically higher due to limb brightening and our non-perfect account for illumination as $1/\mu_0$. Because of that, we ignored the high-latitude data points and fitted the phase functions to the lower-latitude data points (green to blue in the left panels of Fig. 2). The Henyey-Greenstein curve fits for the local pixel brightness values in the left panels (input to our disk-averaging model) were also tuned such that the the disk-integrated brightness curves in the right panels (output from the model) fits the disk-averaged blue data points measured from the Cassini full-disk images. The full-disk images were taken during October, 2000 – March, 2001 flyby. We use images with spatial resolutions ranging ∼200 to ∼2000 km/pixel to compute the full-disk albedo. The images are calibrated by the Cassini ISS CALibration software (CISSCAL) (West et al., 2010)[1]. We compute the full-disk albedo by the ratio between the disk-integrated ISS irradiance and the disk-integrated referenced solar spectral irradiance[2] for different Cassini filters. The phase angle changes from 0° to ∼141°

[1]CISSCAL performs standard CCD calibration such as bias/dark subtraction, flatfield correction, and ISS-specific calibrations. The ground-based observations (Karkoschka 1998) are used to improve the calibration in CISSCAL. We use CISSCAL output of absolute reflected solar irradiance in units of photons/second/cm^2/nm/steradian at the wavelengths bands of Cassini filters.

[2] The referenced solar spectral irradiance comes from a combination of the observations from the Upper Atmosphere Research Satellite (UARS) and the Solar Radiation and Climate Experiment (SORCE). The UARS made the observations from 1991 to 2001, which includes the time period of the Cassini Jupiter flyby. The spectral coverage of the UARS (22-420 nm) does not include the long visible wavelength (420-1000 nm). The SORCE has a better spectral coverage (0.5-2400 nm). But the SORCE began in 2003, afrer the Cassini Jupiter flyby (2000-2001). We first average the UARS solar spectral irradiance from October 2000 to March 2001 at the short visible wavelengths (22-420 nm). Then, we scale the SORCE solar spectral irradiance at the long visible wavelengths (420-1000 nm) in 2003 to the time of the Cassini Jupiter flyby by the ratio of integrated solar irradiance at the short visible wavelength (22-420 nm) between the SORCE and the UARS. Finally, we combine the UARS and the SRCE data as the reference solar spectral irradiance and multiply it by the area of Jupiter disk. The observed solar spectral irradiance at each pixel is multiplied by the area of the pixel, and summed over all pixels in the full-disk images.

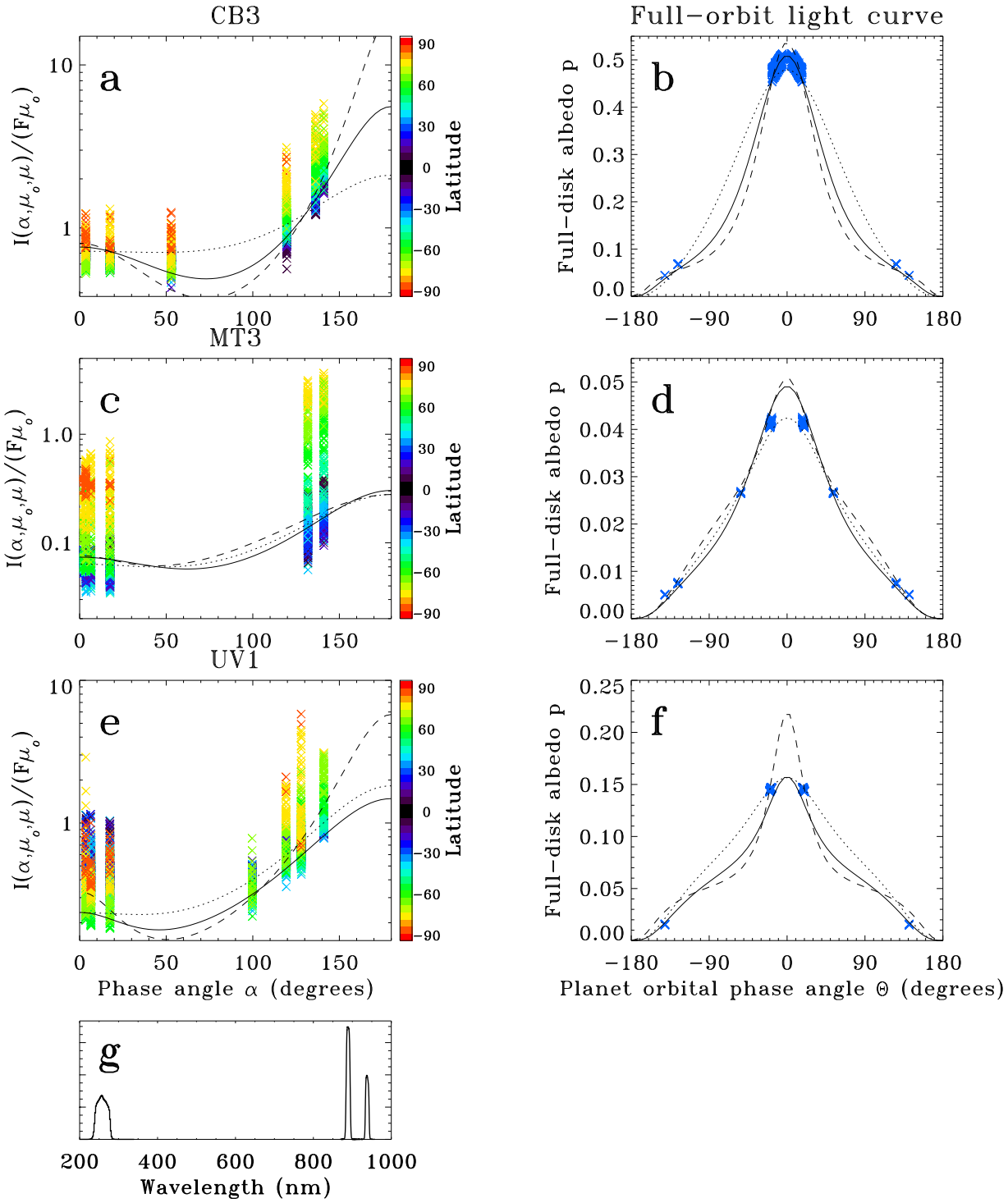

Fig. 2.— Henyey-Greenstein functions (curves in panels a, c, e with linestyles corresponding to Table 2) fitted to pixel brightness in the images taken by Cassini during its flyby of Jupiter in 2000-2001. Panels a,c,e represent images taken with Cassini NAC camera filters: CB3, MT3, and UV1 as labeled on top of the plots. The same data were used to model atmospheric aerosols by (Zhang et al. 2013). The right panels (b, d, f) show the modeled light curves corresponding to the lines in the left panel for each filter. The blue × symbols show disk-integrated brightness measured from the Cassini images. Panel g shows filter shapes: UV1 at 258 nm, CB3 at 938 nm, and MT3 at 889 nm.

during the flyby, but there are no suitable full-disk images at some phase angels. As a result, there are some gaps in the coverage, different for each filter.

In addition to the Pioneer and Cassini data studied here, images of Jupiter were taken by Voyager, Galileo, and New Horizons, which covered a variety of angles. We are not aware of any other published data of the scattering phase functions for the Jovian surface. Data for α >150° do not exist because these directions would risk pointing spacecraft cameras too close to the Sun. Accordingly, the fitted phase curves at α >150° are not well restricted. However the resulting light curves and spherical albedos are not severely affected by our extrapolation at α >150°. At these angles the observed crescent is narrow, and the total reflected light is small.

2.1.2. Saturn

For Saturn, we use the scattering phase function from Dones et al. (1993) and Dyudina et al. (2005), which depends on three angles: incidence (via μ_0), emission (via μ), and phase angle α. The function is the Backstorm law fitted to Pioneer 11 data by Dones et al. (1993).

$$I/F = \frac{A}{\mu}\left(\frac{\mu \cdot \mu_0}{\mu + \mu_0}\right)^B \quad , \tag{4}$$

where A and B depend on the phase angle α. In this study we use the same functions as in Dyudina et al. (2005). Table 3 lists the Backstorm parameters.

Phase angle α	0°	30°	60°	90°	120°	150°	180°
A (red, 0.64 μm)	1.69	1.59	1.45	1.34	1.37	2.23	3.09
B (red, 0.64 μm)	1.48	1.48	1.46	1.42	1.36	1.34	1.31
A (blue, 0.44 μm)	0.63	0.59	0.56	0.56	1.69	1.86	3.03
B (blue, 0.44 μm)	1.11	1.11	1.15	1.18	1.20	1.41	1.63

Table 3: Coefficients for the Backstorm function for Saturn, from Dones et al. (1993) also used by Dyudina et al. (2005).

2.2. Full-disk and Geometric Albedos.

To produce light curves of the fiducial exoplanets that we model, images of the planet for a set of locations along the orbit are generated using a model by Dyudina et al. (2005).

For each image we integrate the total light coming from the planet to obtain the full-disk albedo $p(\alpha)$.

$$p(\alpha) = \frac{\sum_{\text{pixels}} I(\mu, \mu_0, \alpha) \cdot r_{\text{pix}}^2 / F}{\pi R_P^2} \quad , \tag{5}$$

where r_{pix} is the pixel size and R_P is the planet's radius. Note that $\sum_{\text{pixels}} I(\mu, \mu_0, \alpha) \cdot r_{\text{pix}}^2 = L_P$ is the planet's luminosity. Generally, I, L_P, F, and p depend on wavelength. In our case these values are weighted averages over the Pioneer and Cassini filter passbands (Fig. 2g for Cassini). The commonly-used term "geometric albedo" A_g (measured for extrasolar planets at secondary eclipse) is defined as our full-disk albedo at zero phase angle $\alpha = 0$ (opposition), i.e., $A_g = p(0)$.

3. Light curves

We first tested how light curves would differ for exoplanets with the surface reflection characteristics of Jupiter's, Saturn's, Lambertian, and Rayleigh scattering.

Figure 3a compares surface reflection functions for Jupiter and Saturn for Pioneer and Cassini wavelength bands (fitted to the data in Figs. 1 and 2), for theoretical wavelenght-indepent Lambertian surface, and for Rayleigh-scattering surface. The Rayleigh case was calculated with multiple scattering model VLIDORT (Spurr 2006) applied to a spherical planet similarly to results of Kopparla et al. (2015), who used the quadrature method of Horak (1950) for disk integration. Note the logarithmic scale of the ordinate and the large amplitudes of the phase functions.

Figure 3b compares edge-on light curves for spherical same-size planets on circular orbits. Their surface reflection properties correspond to panel a. The luminosity of the planet is normalized by the incident stellar light to obtain the full-disk albedo p as described in equation (5). The full-disk albedo can be converted into the planet's luminosity L_P as a fraction of star's luminosity L_* for a planet of radius R_P at an orbital distance D_P.

$$L_P / L_* = (R_P / D_P)^2 \cdot p \tag{6}$$

For example, for Saturn at 1 AU, $(R_P/D_P)^2 \approx 1.6 \times 10^{-7}$. The plot in Fig. 3b can be transformed into a time-dependent light curve simply by dividing orbital phase angle α by 360° and multiplying by the planet's orbital period.

As can be seen in Fig. 3b, the light curves for Jupiter peak more sharply at opposition ($\Theta \approx 0°$) than the light curves of Saturn, Lambertian, or Rayleigh-scattering planet. This reflects the sharp back-scattering peak in Jupiter's surface scattering (at $\alpha \approx 0°$ in Fig. 3a).

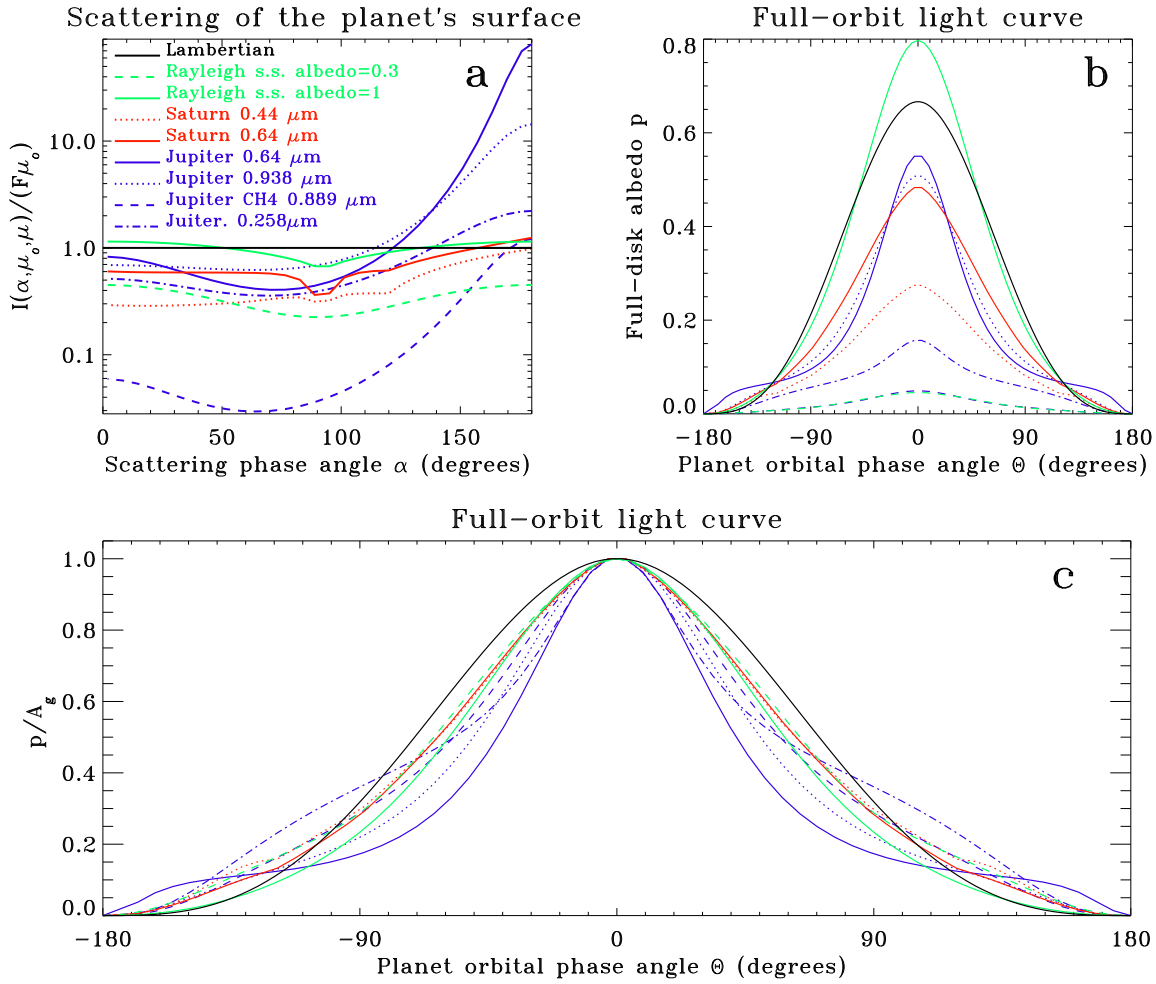

Fig. 3.— Panel a: Surface scattering functions for a Lambertian surface, semi-infinite Rayleigh layer with single scattering albedo 1 (green solid line) and single scattering albedo 0.3 (green dashed line), derived from VLIDORT model (Kopparla et al. 2015)), and Saturn and Jupiter at several wavelengths. The linestyles are different from notation in Section 2. Here the linestyles represent wavelength bands. For each wavelength only one curve labeled "solid" in Section 2 is plotted in this figure as dashed, dotted or dot-dashed (see labels in paned a). The phase functions in panel a are plotted for a specific geometry in which the Sun is 2° above the horizon (μ_0=0.035) and the observer moves from the Sun's location ($\alpha = 0°$) across the zenith toward the point on the horizon opposite to the Sun ($\alpha = 178°$). Panel b: Comparison of light curves for a spherical planet assuming scattering properties from panel a. The linestyles and colors correspond to panel a. Panel c: Same as panel b but all the curves are normalized by their geometric albedo $A_g \equiv p(0)$.

The peak is probably the result of scattering by large cloud particles. It should be noted though that Rayleigh scattering atmosphere (green curves in Fig. 3) can also produce sharper peaks than in Lambertian case, as previously modeled by Madhusudhan and Burrows (2012). As seen in Fig. 3c, the peaks in the light curves for Jupiter (blue lines) are much sharper than the ones expected from Rayleigh scattering (green lines).

The variety of light curve shapes in Fig 3c shows the uncertainty range when gaseous planets are described by simple Lambertian approximation. For example, some Jupiter's light curves would be a factor of two fainter at half phase ($\alpha \approx \pm 90°$) than Lambertian curve, given the same geometric albedos at secondary eclipse ($\alpha = 0°$). Also, near the transit ($\alpha \approx \pm 180°$), Lambertian curve is much fainter than any of the more realistic light curves. This shows the importance of the forward-scattering atmospheres for the light curves near the transit.

4. Total Reflection from the Planet

The total reflected light from the planet can be obtained by integrating the reflected light in all directions and wavelengths. The result divided by the incident solar flux is called Bond albedo A_b. A_b is usually estimated from observable geometric albedo A_g at particular wavelength band, extrapolated over wavelengths and over different directions. Lambertian assumption is commonly used, which, as we show here, is likely to overestimate Bond albedo.

At specific wavelength, the reflection of the planet's surface is defined by its spherical albedo A_S.

$$A_S = \int_0^{4\pi} p(\alpha) d\Omega, \tag{7}$$

where the reflection from the planet is integrated over all outgoing solid angles Ω. In general case p also depends on the azimuth of the observer relative to the planet. In our simplified case $p(\alpha)$ depends only on phase angle α, and A_S can be converted to an integral over α (see also Eq. 3.29 of Seager and Deming (2010), where $\Psi = \pi \cdot p(\alpha)$).

$$A_S = 2 \int_0^{\pi} p(\alpha) sin(\alpha) d\alpha, \tag{8}$$

The absorbed light for the planet, as a fraction of incident light, is $1 - A_S$. In Lambertian case the integral over α can be solved analytically giving theoretical ratio of spherical to geometric albedo, or phase intergal A_S/A_g:

$$A_S = \frac{3}{2} p(\alpha = 0) = \frac{3}{2} A_g \tag{9}$$

We calculate spherical albedos in the observed spacecraft filter bands to estimate how Lambertian approximation can can over- or under-estimate the conversion from geometric to Bond albedo, which is typically used to estimate the stellar heating for extrasolar planets. Table 4 lists geometric and spherical albedos derived in our models. We also list the phase integral A_S/A_g, to compare it with previous results. The phase integral had been estimated before from Pioneer images at red and blue wavelengths. A cloud scattering model fitted to Pioneer data gives A_S/A_g=1.2-1.3 for Jupiter (Tomasko et al. 1978), and A_S/A_g=1.4±0.1 for Saturn (Tomasko and Doose 1984). Our estimates, based on the curve fitting to the surface scattering data, are consistent with these values.

Table 4: Geometric and spherical albedos A_g and A_S, and the phase integral A_S/A_g derived for different reflection functions fitted to the data. The fitting uncertainty is indicated by the range of the fitted curves for each filter (solid, dashed, and dotted in Figs. 1 and 2 and Table 2). The coefficient for non-Lambertian correction C is given in the last column.

	Geometric albedo A_g	Spherical albedo A_S	A_S/A_g	C
Lambertian	0.666	1.00	1.50	1.00
Rayleigh semi-infinite s.s. albedo = 1	0.676	0.94	1.40	0.93
Saturn 0.44 (0.39-0.5)μm (Pioneer blue)	0.274	0.39	1.44	0.96
Saturn 0.64 (0.59-0.72)μm (Pioneer red)	0.483	0.67	1.39	0.92
Jupiter 0.64 (0.59-0.72)μm (Pioneer red) solid	0.549	0.56	1.02	0.68
dashed	0.508	0.48	0.95	0.63
dotted	0.560	0.71	1.28	0.85
Jupiter atm. window 0.938μm (Cassini CB3) solid	0.507	0.59	1.17	0.78
dashed	0.534	0.51	0.96	0.64
dotted	0.478	0.75	1.58	1.05
Jupiter CH_4 0.889μm (Cassini MT3) solid	0.048	0.06	1.35	0.90
dashed	0.050	0.07	1.48	0.99
dotted	0.042	0.06	1.62	1.08
Jupiter 0.24-0.28μm (Cassini UV1) solid	0.156	0.23	1.47	0.98
dashed	0.217	0.22	1.04	0.69
dotted	0.156	0.29	1.85	1.23

The phase integrals in Table 4 are useful for understanding realistic conversion from geometric to Bond albedo A_b/A_g. With the lack of spectral information, A_b can be estimated from geometric albedo measured at particular wavelength assuming A_g and A_S are constant with wavelengths. Then the Bond albedo, averaged over wavelengths, can be roughly

approximated by spherical albedo: $A_b \sim A_S$.

Looking at the phase integral A_S/A_g at different wavelength in Table 4, one can get a feel of the range of possible A_b/A_g ratios for Saturn- and Jupiter-like atmospheres. Because the typical assumption for exoplanet reflectance calculation is Lambertian ($A_S/A_g = 3/2$), we calculate a correction coefficient C that gives an overestimate which Lambertian assumption imposes on the total planet's reflection when it is derived from geometric albedo.

$$C = \frac{(A_S/A_g)}{(A_S/A_g)_{Lambertian}} = \frac{2(A_S/A_g)}{3} \tag{10}$$

To correct the spherical albedo derived under Lambertian assumption $A_S(Lambertian)$ for realistic anisotropic scattering, it should be multiplied by $A_S = C \cdot A_S(Lambertian)$. Similar correction for wavelength-averaged Bond albedo is probably in the range of correction coefficients for different wavelength bands in Table 4. Table 4 shows that it may be as low as C =0.68, which means Lambertian assumption gives an overestimate for A_S by a factor of $1/0.68 \approx 1.5$.

To put it in the context of exoplanets, for planet HD 189733b, having $A_g \approx 0.4$ at blue wavelengths (Evans et al. 2013), would mean that instead of 40% of stellar light ($1 - A_S(Lambertian) = 1 - A_g \times (A_S/A_g)_{Lambertian} = 1 - 0.4 \times 1.5 = 40\%$) the planet absorbs about 60% ($1 - A_S(Lambertian) \times 0.68 \approx 60\%$).

5. Discussion

This research presents the summary of Jupiter's and Saturn's cloud reflection properties at different wavelengths and illumination phases in a form of simple analytical functions fitted to the observations. These summarized observations can be easily used by those who model cloud scattering on extrasolar planets to test their models on Jupiter and Saturn data.

We derived light curves consistent with Jupiter's and Saturn's spacecraft observations. To do that we used the direct measurements from full-disk spacecraft images, and, where such images are not available, extrapolation of this data with a disk-averaging model that converts partial-disk images to full-disk.

The light curves for the cloudy atmospheres of Jupiter and Saturn (Fig. 3) show considerably different shape than the Lambertian light curve. A factor of few differences in amplitude are expected at phases different from secondary eclipse, which may be detectable in the near future. Especially interesting for exoplanet studies is the high brightness due to

forward scattering near the transit, which is not present in the Lambertian case. However, this forward-scattering effect is not well restricted by the data on Jupiter and Saturn because the spacecraft avoid pointing too close to the Sun to prevent the detectors from overheating.

The total reflected flux from the planet judjed by geometric albedo also depends on forward and backward scattering. From variety of wavelength bands studied (Table 4), the effect is between factor of 0.6 and 1.2 (values of C in Table 4). This tells us that the Lambertian approximation is probably a reasonable one to use for cloudy planets, given the observational error bars on geometric albedos for extrasolar planets.

Solid planets are expected to have much stronger opposition effect (e.g., for Galilean satellites, Domingue and Verbiscer 1997), which is likely to distort the shape of the light curve more strongly than for the cloudy planets, and also to have a stronger effect on the estimated planet's reflected light.

Acknowledgements

This research was supported by the NASA Cassini Project. We thank R.A. West for comments on the manuscript and references on Jupiter's scattering. We thank S.P. Ewald for the comments on the manuscript.

REFERENCES

Cowan, N. B., Agol, E., Charbonneau, D., 2007. Hot nights on extrasolar planets: mid-infrared phase variations of hot Jupiters. MNRAS 379, 641–646.

Demory, B.-O., de Wit, J., Lewis, N., Fortney, J., Zsom, A., Seager, S., Knutson, H., Heng, K., Madhusudhan, N., Gillon, M., Barclay, T., Desert, J.-M., Parmentier, V., Cowan, N. B., 2013. Inference of Inhomogeneous Clouds in an Exoplanet Atmosphere. ApJ 776, L25.

Domingue, D., Verbiscer, A., 1997. Re-Analysis of the Solar Phase Curves of the Icy Galilean Satellites. Icarus 128, 49–74.

Dones, L., Cuzzi, J., Showalter, M., 1993. Voyager photometry of saturn's a ring. Icarus 105, 184–215.

Dyudina, U. A., Sackett, P. D., Bayliss, D. D. R., Seager, S., Porco, C. C., Throop, H. B.,

Dones, L., 2005. Phase Light Curves for Extrasolar Jupiters and Saturns. ApJ 618, 973–986.

Evans, T. M., Pont, F., Sing, D. K., Aigrain, S., Barstow, J. K., Désert, J.-M., Gibson, N., Heng, K., Knutson, H. A., Lecavelier des Etangs, A., 2013. The Deep Blue Color of HD 189733b: Albedo Measurements with Hubble Space Telescope/Space Telescope Imaging Spectrograph at Visible Wavelengths. ApJ 772, L16.

Harrington, J., Hansen, B. M., Luszcz, S. H., Seager, S., Deming, D., Menou, K., Cho, J. Y.-K., Richardson, L. J., 2006. The Phase-Dependent Infrared Brightness of the Extrasolar Planet υ Andromedae b. Science 314, 623–626.

Heng, K., Demory, B.-O., 2013. Understanding Trends Associated with Clouds in Irradiated Exoplanets. ApJ 777, 100.

Horak, H. G., 1950. Diffuse Reflection by Planetary Atmospheres. ApJ 112, 445.

Karkoschka, E., 1994. Spectroscopy of the jovian planets and Titan at 300- to 1000-nm wavelength: The methane spectrum. Icarus 111, 174–192.

Karkoschka, E., 1998. Methane, Ammonia, and Temperature Measurements of the Jovian Planets and Titan from CCD-Spectrophotometry. Icarus 133, 134–146.

Knutson, H. A., Charbonneau, D., Allen, L. E., Fortney, J. J., Agol, E., Cowan, N. B., Showman, A. P., Cooper, C. S., Megeath, S. T., 2007. A map of the day-night contrast of the extrasolar planet HD 189733b. Nature 447, 183–186.

Kopparla, P., Natraj, V., Zhang, X., Swain, M. R., Wiktorowicz, S. J., Yung, Y. L., 2015. A multiple scattering radiative transfer model for interpreting exoplanetary polarimetric observations. submitted.

Madhusudhan, N., Burrows, A., 2012. Analytic Models for Albedos, Phase Curves, and Polarization of Reflected Light from Exoplanets. ApJ 747, 25.

Madhusudhan, N., Knutson, H., Fortney, J., Barman, T., 2014. Exoplanetary Atmospheres. ArXiv e-prints.

Porco, C. C., West, R. A., Squyres, S., McEwen, A., Thomas, P., Murray, C. D., Delgenio, A., Ingersoll, A. P., Johnson, T. V., Neukum, G., Veverka, J., Dones, L., Brahic, A., Burns, J. A., Haemmerle, V., Knowles, B., Dawson, D., Roatsch, T., Beurle, K., Owen, W., 2004. Cassini Imaging Science: Instrument Characteristics And Anticipated Scientific Investigations At Saturn. Space Sci. Rev. 115, 363–497.

Schwartz, J. C., Cowan, N. B., 2015. Balancing the energy budget of short-period giant planets: evidence for reflective clouds and optical absorbers. MNRAS 449, 4192–4203.

Seager, S., Deming, D., 2010. Exoplanet Atmospheres. ARA&A 48, 631–672.

Smith, P. H., Tomasko, M. G., 1984. Photometry and polarimetry of jupiter at large phase angles. ii polarimetry of the South Tropical Zone, South Equatorial Belt, and the polar regions from the Pioneer 10 and 11 missions. Icarus 58, 35–73.

Spurr, R. J. D., 2006. VLIDORT: A linearized pseudo-spherical vector discrete ordinate radiative transfer code for forward model and retrieval studies in multilayer multiple scattering media. J. Quant. Spec. Radiat. Transf. 102, 316–342.

Tomasko, M. G., Doose, L. R., 1984. Polarimetry and photometry of Saturn from Pioneer 11 Observations and constraints on the distribution and properties of cloud and aerosol particles. Icarus 58, 1–34.

Tomasko, M. G., West, R. A., Castillo, N. D., 1978. Photometry and polarimetry of Jupiter at large phase angles. I. Analysis of imaging data of a prominent belt and a zone from Pioneer 10. Icarus 33, 558–592.

West, R. A., Baines, K. H., Friedson, A. J., Banfield, D., Ragent, B., Taylor, F. W., 2004. *Jupiter. The Planet, Satellites and Magnetosphere*, Chapter Jovian clouds and haze, pp. 79–104. Cambridge Univ. Press.

West, R. A., Baines, K. H., Karkoschka, E., Sánchez-Lavega, A., 2009. *Saturn from Cassini-Huygens*, Chapter Clouds and aerosols in Saturn's atmosphere. Springer.

Zhang, X., West, R. A., Banfield, D., Yung, Y. L., 2013. Stratospheric aerosols on Jupiter from Cassini observations. Icarus 226, 159–171.